



PHOTONICS Research

Cavity continuum

FAN CHENG,¹ VLADIMIR SHUVAYEV,² MARK DOUIDZON,³ LEV DEYCH,⁴ AND TAL CARMON^{1,*}

¹School of Electrical Engineering, Tel Aviv University, Tel Aviv 6997801, Israel

²Physics Department, Queens College of CUNY, Flushing, Queens, New York 11367, USA

³Solid State Institute, Technion-Israel Institute of Technology, Haifa 3200003, Israel

⁴The Graduate Center of CUNY, New York, New York 10016, USA

*Corresponding author: total@tauex.tau.ac.il

Received 13 September 2023; revised 13 December 2023; accepted 13 December 2023; posted 13 December 2023 (Doc. ID 505164); published 8 February 2024

We experimentally demonstrate and numerically analyze large arrays of whispering gallery resonators. Using fluorescent mapping, we measure the spatial distribution of the cavity ensemble's resonances, revealing that light reaches distant resonators in various ways, including while passing through dark gaps, resonator groups, or resonator lines. Energy spatially decays exponentially in the cavities. Our practically infinite periodic array of resonators, with a quality factor (Q) exceeding 10^7 , might impact a new type of photonic ensembles for nonlinear optics and lasers using our cavity continuum that is distributed, while having high- Q resonators as unit cells. © 2024 Chinese Laser Press

<https://doi.org/10.1364/PRJ.505164>

1. INTRODUCTION

High- Q optical resonators [1,2] supported microlasers [3–8], nonlinear optics [9,10], and experiments in cavity optomechanics [11] and optocapillaries [12]. As one can see in Fig. 1, optical resonators were extended to an array of a few and then several resonators. Here we mass-produce microdroplet resonators with optical Q exceeding 10^7 and cascade them into a cavity continuum of practically unlimited size. In detail, coupling between a pair of resonators permitted enhanced sensing using exceptional points [13,24–26]. Cascading three cavities allowed flattened bandpass filters [27]. Then, going to several resonators exhibited families of modes, repeating every free spectral range [14,28]. Clusters of five microparticles [15], each with Q near 1000, allowed biosensing via the ensemble's spectral fingerprint. Massive 3D arrays of dielectric microspheres with many resonators and $Q = \sim 1000$ were exhibiting anomalously high transmission at the whispering gallery mode (WGM) peak wavelengths [16]. On another extreme, random lasers [29–32] represent a structure where coincident multiscattering, e.g., by porous media, provides feedback, while each scatterer is a nonresonant body or, in different words, with a very low Q , typically near 1. As for the arrangement of resonators [33,34], cavities can be coupled in a linear array [14,17,35,36], branched structures [18,37], 3D structures [16,38,39], and a close-packed layer that we present here.

Here we introduce and study a continuous resonator array. This type of cavity continuum might support detection via the ensemble's spatial and spectral fingerprint [15] at higher Q , benefiting better sensitivity to analytes. This cavity ensemble might also permit a new type of random lasers [29–32], and

delay lines [34], or enable phase matching for nonlinear effects via a denser power spectrum [7]. In a broader context, one can describe our cavity continuum as a new type of photonic ensembles where each unit cell is a spherical resonator with Q exceeding 10^7 .

Droplets were functioning as optical cavities with high Q [12,19,40–43] and activated as Raman [44], Brillouin [45], and water-wave lasers [46]. Coupling between resonators requires nanometer-scale control over the distances between resonators, which is challenging. Nevertheless, droplet resonators are relatively easy to mass-produce [47–50] and self-arrange into a periodic array of almost touching droplets. Despite that, coupling many high- Q microresonators into a continuous array was rarely studied, not even theoretically [51–53]. Following the recent demonstration of optical coupling between several droplet resonators [14], we extend this ensemble here to a cavity continuum that is practically unlimited in size. The current practical limit on the size of our array is near 400, limited by the sensitivity of our camera.

We examine the optical modes of the resonator ensemble using the fluorescent mode mapping technique. In detail, doping the liquid surrounding the droplets with a fluorescent material makes this region glow in places where the droplet's mode evanescently extends to its surroundings. We can therefore perform a wavelength scanning of the input light while taking a movie of the fluorescent emission. The micrographs representing the movie's frames reveal the resonance's spatial structure, while the time variation of the emission from each resonator represents its optical absorption. In this manner, the fluorescent-based technique maps resonances both spatially

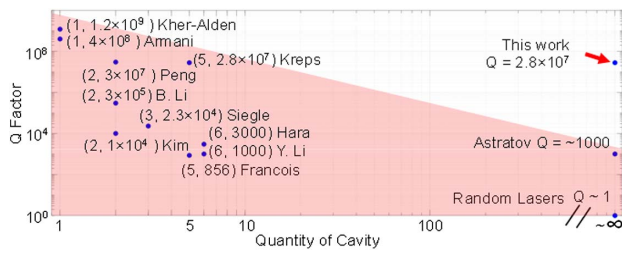


Fig. 1. Number of microresonators versus Q factor [13–23] represents a trade-off between the quality factor and the number of resonators. Our work on the top right uniquely combines high optical Q with a large number of resonators.

and spectrally. It is helpful that fluorescent dopants convert some of the coherent resonance light into incoherent radiation emitted in all directions. This is because, unlike coherent light, fluorescent emission does not suffer speckles and is therefore benefitting higher quality images. Such fluorescence was used to map the modes of spherical resonators [3,4] as well as for measuring stopped light in such spheres [54]. In toroids, level-crossing phenomena were fluorescently photographed [55], and in liquid droplets, fluorescent mapping resolved the structure of droplet WGMs [56], as well as of the fluidic vortices [57] they generate. In a similar manner, the optical modes of a water fiber were mapped [58]. Later on, modes of a few-droplet ensemble [14] were fluorescently mapped.

2. EXPERIMENTAL SETUP

In our experimental setup, as depicted in Fig. 2, we employ a 780 nm tunable laser (New Focus, TLB-6712-P) as a light source. We use a curved tapered fiber to couple light into the droplets. A straight tapered fiber is fabricated by heating a single-mode fiber (Thorlabs, 780HP) with a hydrogen flame while drawing it with two translation stages. To make this taper bent [60], for the purpose of accessing only several droplets, we release the straight tapered fiber to generate a curved variant and heat it again for annealing, producing a mechanically stable fiber [61]. The curved tapered fiber is rotated by two fiber rotators (Thorlabs, HFR007) until the curved part faces downwards. This can allow the thinnest part to touch a few droplets while the tapered regions are far from obstacles. Droplet generation is explained in Appendix A.

The curved tapered fiber is positioned in a chamber constructed from two cover slices and a glass slide (thickness: 1 mm), which is filled with deionized water and fluorescent dye (American Dye Source Inc., ADS780WS, 3 $\mu\text{mol/L}$ [56], absorption peak at 780 nm, emission peak at 813 nm, as shown in Fig. 11 Appendix B). The chamber can maintain a relatively stable aquatic environment due to the water's surface tension, preventing leakage around the edges. The fluorescent dye is dissolved into the deionized water to be later used for mapping the optical mode. To distinctly observe the fluorescence and eliminate the scattering of the laser, a long pass filter (Thorlabs, FELH0800, cut-on wavelength: 800 nm) is inserted between a vertical microscope and a near-infrared (NIR) camera (Lumenera, Infinity 3S) (Appendix B).

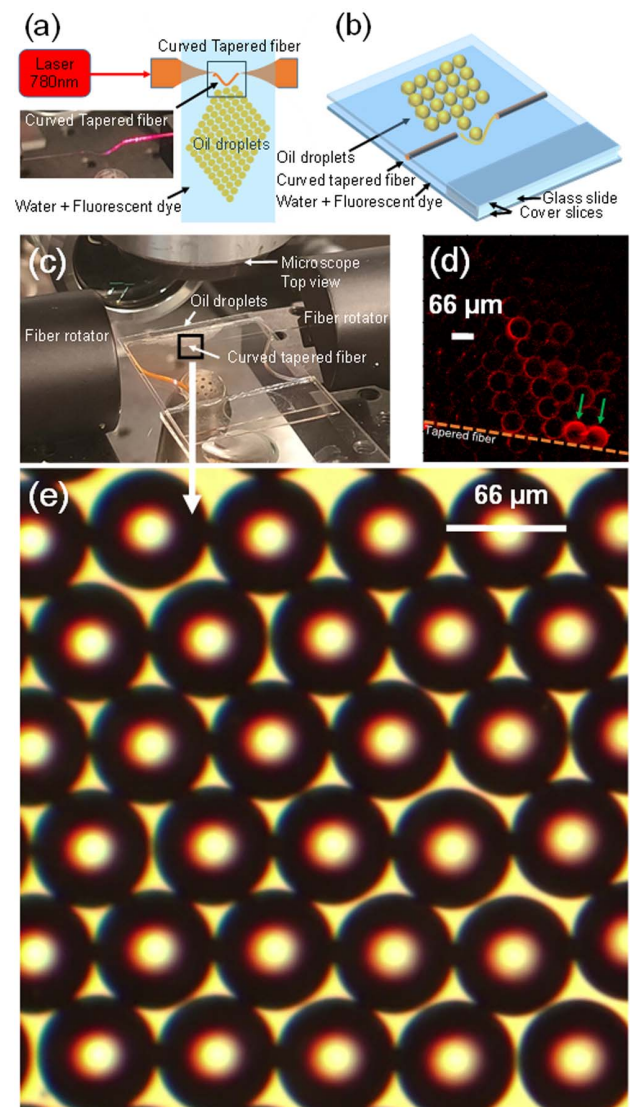


Fig. 2. Coupling setup. (a) A tunable laser (780 nm) serves as the laser source, and a curved tapered fiber is used to couple oil droplets. (b) A chamber is assembled by two cover slices and a glass slide (thickness: 1 mm). The chamber is filled with deionized water and fluorescent dye. The oil droplets are placed in the water environment to maintain their spherical shape. The fluorescent dye is used for mapping the mode. (c) A vertical microscope is used to observe the coupled droplets. Two fiber rotators are used for the fabrication of the curved tapered fiber. (d) A top view image taken by the vertical microscope and a near-IR camera reveals coupled droplets with a highlighted circumference, with the orange dashed line representing the curved tapered fiber. The coupled resonators are marked by green arrows. (e) The clusters are spatially oriented in a hexagonal lattice configuration [59], where the standard deviation in droplet diameter is 0.5 μm and the standard deviation in resonator-to-resonator distance is 1.5 μm . Each droplet is coupled to the other six droplets with 84% success, as indicated by occasional gaps between droplets.

A pipette is employed to transfer the oil droplets to the edge of the chamber, where the droplets spread to form 2D ensembles of droplets. The chamber is fixed onto a translation stage (PI, microtranslation stages, M-105; nanocube nanopositioner:

P-611.3), facilitating the control of the relative positioning between the droplets and the tapered fiber. The droplets are brought close to the thinnest part of the fiber while ensuring the fiber is situated at the same level as the equatorial plane of the droplets. This alignment allows the optical modes of the multiple mutually coupled droplets to maintain a shared plane that runs parallel to the base of the chamber, thereby accomplishing the coupling among multiple droplets. Two droplets are coupled by the tapered fiber [the coupled resonators are marked in Fig. 2(d) by green arrows].

3. EXPERIMENTAL RESULTS

Droplets of uniform size are self-arranged in a periodic array on a 2D plane while interconnected at their equatorial planes. We start by fluorescently mapping a cavity continuum [Fig. 3] by measuring its spectral transmission response in combination with the spatial mode structure for each of the absorption peaks. The fluorescent intensity as a function of time [Fig. 3(a)] stands for the spectral absorption of the cavity continuum and exhibits several absorption lines with $Q = (4.3 \pm 1.1) \times 10^5$. We note that the quality factor of the bare resonators (without the fluorescent ink) exhibits Q exceeding 10^7 , as indicated by the resonance linewidth. Micrographs corresponding to individual absorption peaks are shown in Fig. 3(b) (M1–M9) and represent the spatial distribution of light for these absorption peaks [Fig. 3(a)]. One of the micrographs (M6) [Fig. 3(c)] is enlarged to resolve level crossing between modes frequently, as indicated by a flower-shaped resonance—representing optical interference between two modes having similar resonance frequencies but a different number of wavelengths along the equator line [54–56]. For example, resonator $(-4, 2)$ in Fig. 3(c) has 10 maxima along its circumference arranged in a shape that resembles petals. Given the parameters of the resonator, these 10 circumferential fringes are most likely originating from interference between a mode with 395 waves resonating along the circumference and a mode with 405 circumferential waves. These modes are resonating at the same frequency, to within the resonance full width at half maximum. Though modes of different principal quantum numbers, as in Fig. 3(c) resonator $(-4, 2)$, are expected to resonate at different frequencies, other eigenindices of the modes (e.g., its radial index) can compensate for this spectral gap. As one can see in Fig. 3(b), each of the M1–M9 modes has a unique spatial signature.

We will now measure the spectral properties of an individual resonator in parallel with photographing the spatial distribution of light in the ensemble while this specific cavity is resonating (Fig. 4). This will tell us about the various ways light can reach a specific region of the ensemble. To do so objectively, we photograph a picture at a spectral wavelength supporting a resonance and mark a region of interest (ROI) [Figs. 4(a)–4(c) blue rectangle] that includes a single resonator. We check for the autocorrelation of this ROI photograph with each of the movie frames (Appendix C). The strongest autocorrelation peaks indicate this specific resonator's excitation, as shown in Fig. 4(d). Figures 4(a)–4(c) show the spatial distribution of light corresponding to these correlated absorption peaks. As one can see in Figs. 4(a)–4(c), light can reach the resonator through a row of resonators, through a group of resonators, and, maybe

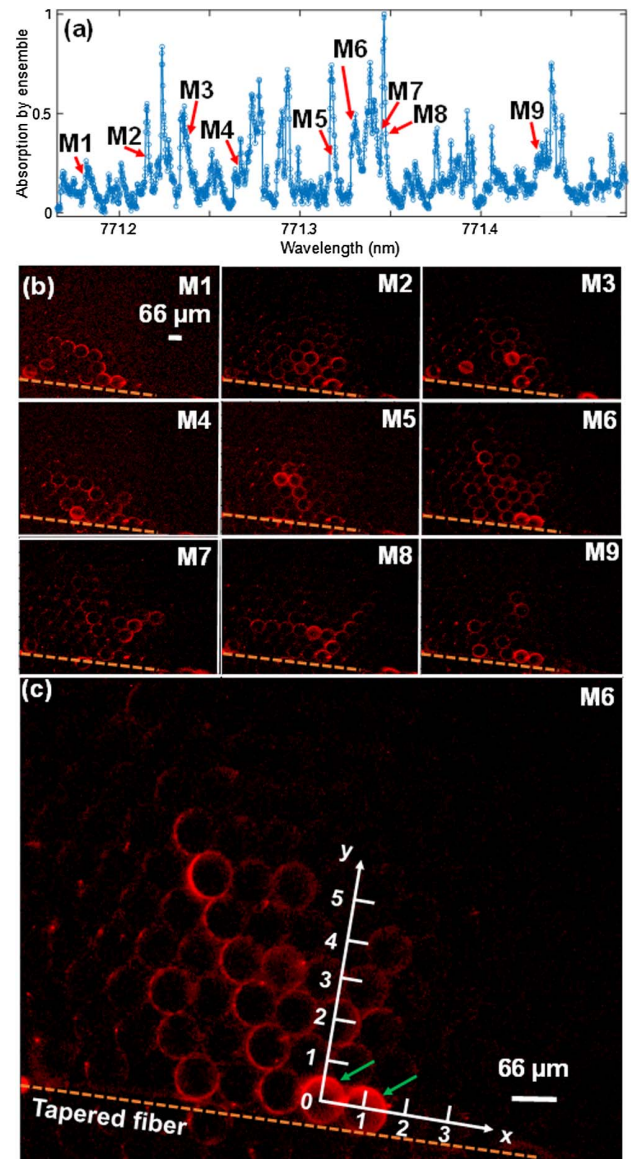


Fig. 3. Fluorescent mode mapping of a cavity continuum. (a) Spectral mapping of the ensemble's absorption lines as indicated by its total fluorescent emission. Several absorption lines are chosen to be accompanied by their spatial mapping (b) as correspondingly indicated in micrographs M1–M9. (c) Ensemble's mode structure with level-crossing events in resonators $(-2.5, 1)$, $(-4, 2)$, $(-2, 2)$, $(-3, 4)$, and $(-4, 6)$. The coupled resonators are marked by green arrows. The orange dashed line represents the curved tapered fiber. The wavelength scan took 30 s (see Visualization 1).

surprisingly, through dark resonators. The quality factor of the individual resonator is $(4.5 \pm 1.5) \times 10^5$, which is slightly higher than the quality of the ensemble (Fig. 3). There exist two possible mechanisms of the optical transports in the arrays of microspheres: evanescent coupling of the WGMs, which might result in the formation of the collective modes of the arrays [17,51,52] and so-called photonic nanojets [62–64]. The latter is a nonresonant phenomenon resulting from focusing of an incident light beam on the shadow side of a microsphere. The authors of Refs. [65–68] showed that such

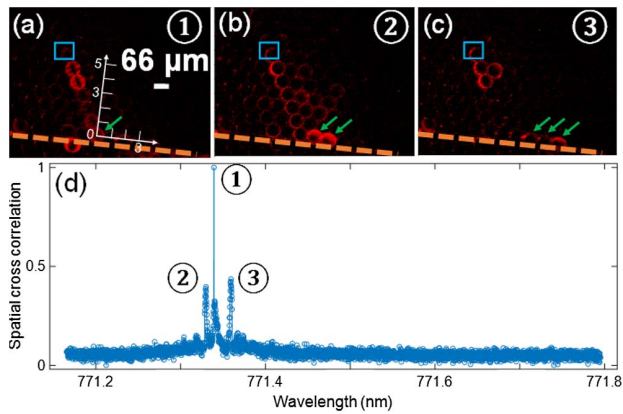


Fig. 4. Ways for light to reach a resonator [marked by the blue rectangle, coordinates $(-3, 5.5)$] (a) through a row of resonators, (b) through a group of resonators, (c) through dark resonators, and (d) correlation between modes. The orange dashed line represents the curved tapered fiber. The wavelength scan took 60 s (see Visualization 1). The coupled resonators are marked by green arrows.

photonic jets can propagate along a long chain of microspheres. There are strong indications that the optical transport observed in our experiments is due to evanescent coupling rather than nanojets. Indeed, nanojets are usually excited by a free propagating light beam or as in the case of Ref. [65] by a broadband fluorescence from an adjacent sphere, while the excitation mechanism in our experiments involves a tapered fiber, which selectively excites only a small number of WGMs, and thus cannot excite photonic jets. The main impediment to the optical transport due to the evanescent coupling is the variation of the sizes of the spheres resulting in the frequency mismatch between resonators. In our experiments, however, the size dispersion of the droplets is less than 1%, which according to Ref. [53] would have resulted in a linear chain of resonators to the localization length of the order of tens of resonators. Moreover, the evanescent transport in our system can be further enhanced due to the relatively large size of the droplets. Indeed, resonators with larger diameters are characterized by a smaller free space region. As a result, WGM with different orbital numbers can spectrally overlap in spheres with different diameters, providing an efficient coupling even between size-mismatched droplets.

To support our experimental findings, we also carried out numerical simulations of an array of resonators. Since simulating numerous coupled 3D droplet resonators using the finite element method encounters significant computational difficulties, we limited our simulations to an array of 2D disk resonators shown in Fig. 5 with a single resonator coupled to the waveguide. Simulations were performed within the regions close to the surface of resonators inside and outside, and the widths of the regions were chosen to keep the light propagation unaffected by the boundaries. We considered an array of 25 closely packed disks arranged in the form of a parallelogram shown in Fig. 5 with the main diagonal at 45° angle with the fiber. The exact orientation of this structure is not significant and is chosen in order to avoid direct excitation by the fiber of more than one resonator. We also did not incorporate

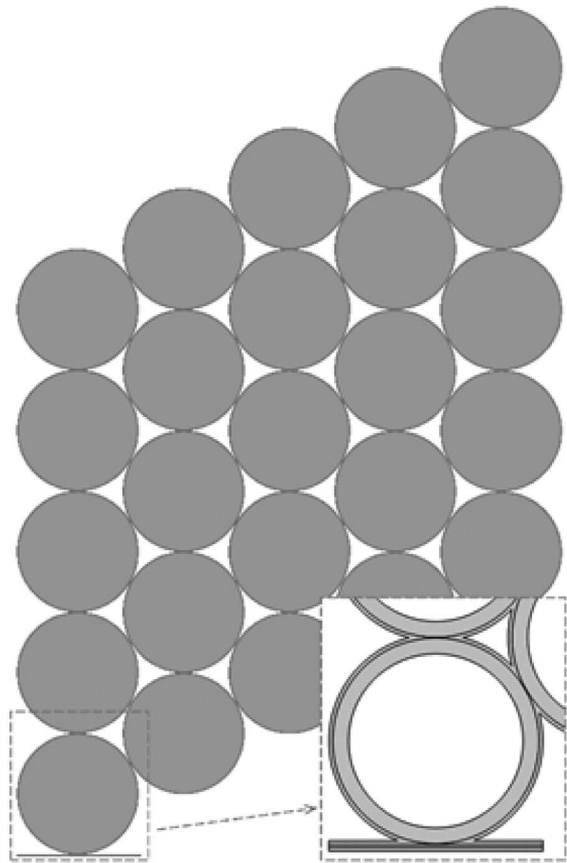


Fig. 5. 2D array of disks with a single disk excited by the waveguide (left-bottom corner of the figure). The inset shows domains where numerical simulations were performed.

in our simulation the variations in the sizes of the disks because this effect was assumed to be small as explained above. This approach is justified by the fact that the goal of the simulations is to demonstrate qualitatively that various propagating paths of light observed in our experiments are real physical phenomena rather than to achieve quantitative agreement between the simulations and the experiment. The later goal would have been unattainable even if we had managed to simulate the actual 3D structures because the exact positions of the droplets in the experiment are not known, while the results of the simulations are sensitive to these parameters. The results of the simulations shown in Fig. 6 reproduce qualitatively various propagating paths of light observed experimentally.

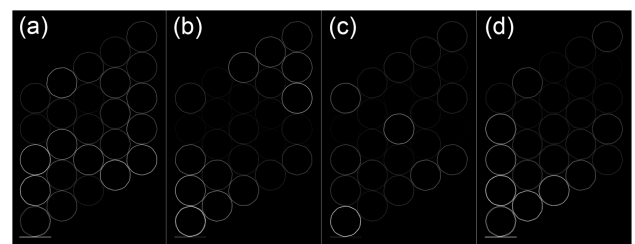


Fig. 6. Various propagating paths of light for different excitation wavelengths. The contrast and brightness of the images were modified to enhance the details of the light distribution.

One of the most interesting configurations observed in real and numerical experiments is the one in which bright resonance is separated by significant dark regions [Fig. 6(b) and Fig. 4(c)]. Similarly, one can see a calculated “V” shaped resonance structure [Fig. 6(d)] and a photograph of its experimentally measured parallel [Fig. 8(a)].

Such a distribution of the intensity can be explained by destructive interference of light taking place within the dark regions between illuminated resonators. This phenomenon can be compared with the distribution of light intensity in a linear chain of resonators studied theoretically in Ref. [35] and experimentally in Refs. [18,37], where certain collective modes of the resonator chains would be characterized by vanishing light intensity inside individual resonators separating brightly lit neighbors.

We will now measure the energy decay as a function of distance from the tapered fiber coupler. We do so by first averaging the movie’s frames while scanning the laser wavelength from 771.0 to 771.6 nm [Fig. 7(a)]. Then we average over all the lines perpendicular to the tapered fiber and fit the intensity decay to an exponential function [Fig. 7(b)]. We see that the decay is exponential, with a characteristic decay distance of 169 μm , meaning that power drops to 37% when reaching this distance from the taper. The number of cavities is limited by the energy decay (Fig. 7) and by camera sensitivity. The exponential decay of the averaged intensity is likely a result of the combination of light attenuation and might be related to Anderson localization of light in this system. While it is not the goal of this paper to study the light localization phenomena, we would like to point out that the coupling between well-confined WGMs is most naturally described in terms of a tight-binding model with nearest-neighbor interaction [2] and both diagonal and nondiagonal disorder. The Anderson localization phenomenon in such models is well established [70]. An alternative approach based on the percolation theory proposed in Ref. [16] can also be used to explain the origin of various paths of light propagation in our system, while our numerical simulation assists with the spatial dependence of the averaged intensity.

As for the size of the cavity continuum, we can now measure—in our experiment, we observed resonances that are excited at a 16-resonator distance from our optical coupler (Fig. 8). Therefore, we are capable of monitoring cavity continuum of $\pi \times 16^2 / 2 = 402$ resonators in a typical experiment. We believe that a cooled CCD and syringe pumps with

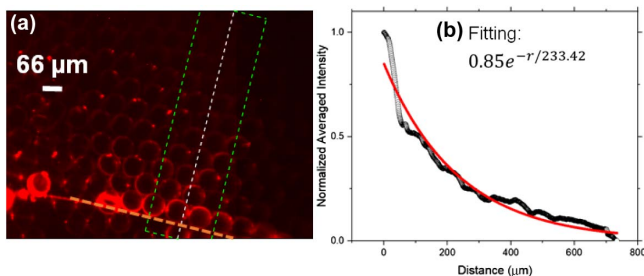


Fig. 7. Energy decay as a function of distance from the tapered fiber. (a) Average of the movie’s frames while the input light is scanning from 771.0 to 771.6 nm. (b) Average over between lines perpendicular to the tapered fiber together with an exponential fit. The orange dashed line represents the curved tapered fiber (see Visualization 2).

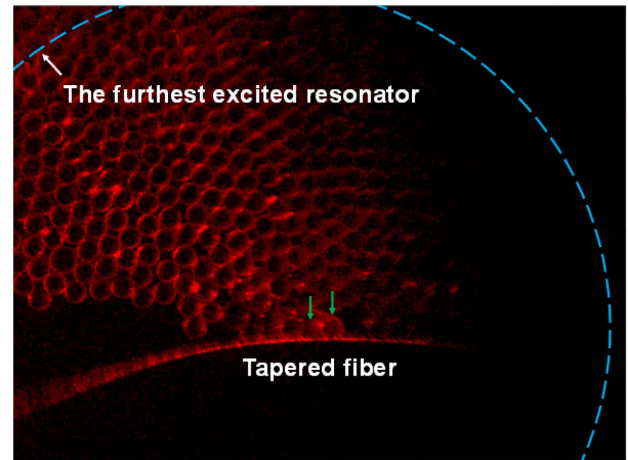


Fig. 8. Cavity number. We could measure a cavity continuum containing 402 resonators. The blue line represents the longest distance from the coupling point, where resonances, in the form of a ring of light appearing upon wavelength scan, were still visible. This blue region contains 402 resonators. This number of cavities is currently limited by our camera sensitivity and droplets’ size variations [69]. The green arrows near the tapered fiber describe the resonators coupled to the tapered fiber.

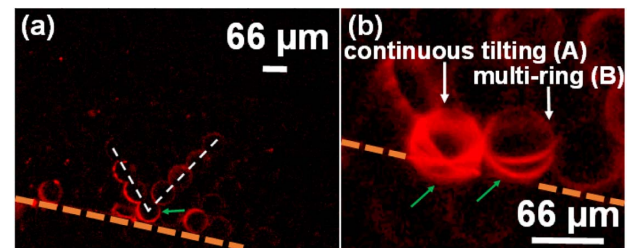


Fig. 9. Variety of mode structures. (a) Collective V-shaped resonance. (b) Individual resonances with multi-ring shapes and continuous tilting during a wavelength scan (see Visualization 2). The orange dashed line represents the curved tapered fiber. The coupled resonators are marked by green arrows.

more stable flow rate for smaller droplets’ size variations, to be implemented in future experiments, will considerably increase the size of the accessible cavity continuum.

Lastly, we depicted photographs describing various spatial structures in the ensemble as well as its individual cavity resonances. Figure 9(a) demonstrates that droplet 1, being in direct contact with the fiber, is coupled to two linear arrays of droplets arranged in a “V” shape. Another coupling phenomenon is observed whereby a single droplet exhibits a resonant structure constructed of rings tilted one in respect to the other [Fig. 9(b)]. Furthermore, as photographed in Fig. 9(b) and a complimentary movie (see Visualization 2), a continuous tilting cycle is observed of the droplet’s mode while we scan the wavelength.

4. CONCLUSIONS

This study optically couples a large number of liquid resonators on a 2D plane via a curved tapered fiber. This new entity is

periodically continuous, as is typical to crystals, with high- Q resonators functioning as unit cells. We believe this study will open a window into a new type of photonic ensembles where many droplets will be arranged in lines, circles, polygons, arbitrary shapes, and various 2D and 3D arrays to investigate new types of photonic continuums.

APPENDIX A: GENERATION OF LIQUID RESONATORS

In the construction of liquid resonators, immersion oil is employed (Sigma, model 56822, $n = 1.516$, 1.025 g/mL). This high-refractive-index oil was selected to provide a large index contrast relative to the surrounding water ($n = 1.333$) to support whispering gallery resonances while suffering minimal optical losses due to radiation [71]. Additionally, this specific oil was chosen for providing quality factors exceeding 10^7 [14]. The liquid resonators are generated using the X-junction of a microfluidic chip (Dolomite, Part number 3000158). As illustrated in Fig. 10, flow rates of oil and deionized water are regulated by two syringe pumps (Chemyx Inc, Fusion 100) (oil, 1 mL syringe, 100 μ L/min; water, 20 mL syringe, 100 μ L/min). The procedure to generate droplets commences with the initiation of the water syringe pump to ensure the entire chip becomes submerged with water, followed by the activation of the oil syringe pump. Inside the chip, the oil phase is subjected to pressure from two water channels, resulting in the generation of oil-in-water droplets. Once a stable production of droplets is confirmed, droplets are subsequently collected in a test tube. This control over flow rates ensures the creation of uniformly sized droplets with a diameter of 66.3 ± 0.5 μ m where accuracy is limited by the resolution of our microscope. Typically, hundredths of thousandths of droplets are generated during a single batch. These droplets, possessing a density greater than that of water, eventually settle at the bottom of the test tube, facilitating the formation of an array where droplet-to-droplet contact is enabled.

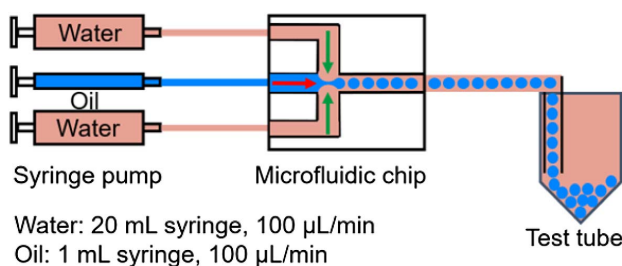


Fig. 10. Droplet generation: schematic diagram of the system generating oil-in-water droplets. Two 20 mL syringes are charged with deionized water, while a 1 mL syringe is filled with immersion oil. The three syringes are propelled at an identical rate of 100 μ L/min. The water acts to compress the oil at the X-junction within a microfluidic chip, thus yielding homogeneous oil-in-water droplets. These collected droplets are then gathered at the base of a test tube due to their higher density compared with water.

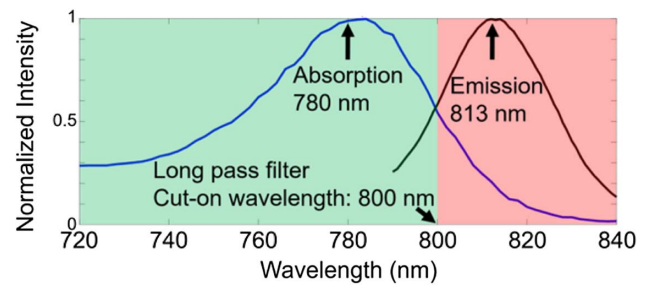


Fig. 11. Fluorescent material properties. (Left) Absorption of the fluorescent material is at the optical resonance wavelengths that we study here. (Right) Fluorescent emission is at a wavelength longer than the cut-on wavelength of the long pass filter, where the NIR CCD camera is still sensitive.

APPENDIX B: FLUORESCENT MATERIAL PROPERTIES

The fluorescent material is dissolved into the deionized water for mapping the optical mode. In Fig. 11, the absorption peak of the fluorescent material is at 780 nm and the emission peak is at 813 nm. A long pass filter is used to distinctly observe the fluorescence and eliminate the scattering of the laser.

APPENDIX C: AUTOCORRELATION

In Fig. 4(d), the normalized intensity of each pixel in the blue rectangle in Fig. 4(a) is multiplied by that of the corresponding pixels in another frame, and then all multiplications are summed to provide the correlation of this specific photograph with the test-case photograph where resonance 7 is excited. This procedure is performed on all of the frames in the movie that is taken during the wavelength scan. The highest peak therefore stands for the modes where resonator number 7 is excited.

Funding. United States–Israel Binational Science Foundation (NSF-BSF) (2020683); Israeli Science Foundation (537/20).

Acknowledgment. We thank Amirreza Ghaznavi, Jie Xu, Yue Wu, Gilad Yossifon, Stanislav Kreps, and Shenglong Liao for their useful technical discussions. F.C. performed the experiments. V.S. performed the theoretical analysis. M.D. and L.D. supervised the work. T.C. supervised all aspects of the work.

Disclosures. The authors declare that there are no conflicts of interest related to this paper.

Data Availability. Data underlying the results presented in this paper are not publicly available at this time but may be obtained from the authors upon reasonable request.

REFERENCES

1. K. J. Vahala, "Optical microcavities," *Nature* **424**, 839–846 (2003).
2. A. B. Matsko and V. S. Ilchenko, "Optical resonators with whispering-gallery modes - Part I: basics," *IEEE J. Sel. Top. Quantum Electron.* **12**, 3–14 (2006).
3. M. Cai, O. Painter, K. J. Vahala, *et al.*, "Fiber-coupled microsphere laser," *Opt. Lett.* **25**, 1430–1432 (2000).

4. L. Yang and K. J. Vahala, "Gain functionalization of silica microresonators," *Opt. Lett.* **28**, 592–594 (2003).
5. T. Carmon, T. Kippenberg, L. Yang, *et al.*, "Feedback control of ultra-high-Q microcavities: application to micro-Raman lasers and microparametric oscillators," *Opt. Express* **13**, 3558–3566 (2005).
6. I. S. Grudinin, A. B. Matsko, and L. Maleki, "Brillouin lasing with a CaF₂ whispering gallery mode resonator," *Phys. Rev. Lett.* **102**, 043902 (2009).
7. M. Tomes and T. Carmon, "Photonic micro-electromechanical systems vibrating at X-band (11-GHz) rates," *Phys. Rev. Lett.* **102**, 113601 (2009).
8. A. Jonáš, M. Aas, Y. Karadag, *et al.*, "In vitro and in vivo biolasing of fluorescent proteins suspended in liquid microdroplet cavities," *Lab. Chip* **14**, 3093–3100 (2014).
9. T. J. Kippenberg, S. M. Spillane, and K. J. Vahala, "Kerr-nonlinearity optical parametric oscillation in an ultrahigh-Q toroid microcavity," *Phys. Rev. Lett.* **93**, 083904 (2004).
10. T. Carmon and K. J. Vahala, "Visible continuous emission from a silica microphotonic device by third-harmonic generation," *Nat. Phys.* **3**, 430–435 (2007).
11. T. Carmon, H. Rokhsari, L. Yang, *et al.*, "Temporal behavior of radiation-pressure-induced vibrations of an optical microcavity phonon mode," *Phys. Rev. Lett.* **94**, 223902 (2005).
12. S. Maayani, L. L. Martin, S. Kaminski, *et al.*, "Cavity optocapillaries," *Optica* **3**, 552–555 (2016).
13. B. Peng, S. K. Özdemir, F. Lei, *et al.*, "Parity-time-symmetric whispering-gallery microcavities," *Nat. Phys.* **10**, 394–398 (2014).
14. S. Kreps, V. Shuvayev, M. Douvidzon, *et al.*, "Coupled spherical-cavities," *AIP Adv.* **12**, 125022 (2022).
15. A. Francois and M. Himmelhaus, "Optical biosensor based on whispering gallery mode excitations in clusters of microparticles," *Appl. Phys. Lett.* **92**, 141107 (2008).
16. V. N. Astratov and S. P. Ashili, "Percolation of light through whispering gallery modes in 3D lattices of coupled microspheres," *Opt. Express* **15**, 17351–17361 (2007).
17. Y. Hara, T. Mukaiyama, K. Takeda, *et al.*, "Heavy photon states in photonic chains of resonantly coupled cavities with supermonodisperse microspheres," *Phys. Rev. Lett.* **94**, 203905 (2005).
18. Y. Li, F. Abolmaali, K. W. Allen, *et al.*, "Whispering gallery mode hybridization in photonic molecules," *Laser Photon. Rev.* **11**, 1600278 (2017).
19. J. Kher-Alden, S. Maayani, L. L. Martin, *et al.*, "Microspheres with atomic-scale tolerances generate hyperdegeneracy," *Phys. Rev. X* **10**, 031049 (2020).
20. D. K. Armani, T. J. Kippenberg, S. M. Spillane, *et al.*, "Ultra-high-Q toroid microcavity on a chip," *Nature* **421**, 925–928 (2003).
21. H.-T. Kim and M. Yu, "Cascaded ring resonator-based temperature sensor with simultaneously enhanced sensitivity and range," *Opt. Express* **24**, 9501–9510 (2016).
22. B. Li, C. P. Ho, and C. Lee, "Tunable Autler–Townes splitting observation in coupled whispering gallery mode resonators," *IEEE Photon. J.* **8**, 4501910 (2016).
23. T. Siegle, S. Schierle, S. Kraemmer, *et al.*, "Photonic molecules with a tunable inter-cavity gap," *Light Sci. Appl.* **6**, e16224 (2017).
24. B. Peng, Ş. K. Özdemir, S. Rotter, *et al.*, "Loss-induced suppression and revival of lasing," *Science* **346**, 328–332 (2014).
25. M. Brandstetter, M. Liertzer, C. Deutsch, *et al.*, "Reversing the pump dependence of a laser at an exceptional point," *Nat. Commun.* **5**, 4034 (2014).
26. H. Hodaie, M.-A. Miri, M. Heinrich, *et al.*, "Parity-time-symmetric microring lasers," *Science* **346**, 975–978 (2014).
27. S. T. Chu, B. E. Little, W. Pan, *et al.*, "Cascaded microring resonators for crosstalk reduction and spectrum cleanup in add-drop filters," *IEEE Photon. Technol. Lett.* **11**, 1423–1425 (1999).
28. V. Shuvayev, S. Kreps, T. Carmon, *et al.*, "Whispering gallery modes of a triatomic photonic molecule," *AIP Adv.* **12**, 115027 (2022).
29. D. S. Wiersma, "The physics and applications of random lasers," *Nat. Phys.* **4**, 359–367 (2008).
30. A. S. Gomes, A. L. Moura, C. B. de Araújo, *et al.*, "Recent advances and applications of random lasers and random fiber lasers," *Prog. Quantum Electron.* **78**, 100343 (2021).
31. T. S. Kao, Y.-H. Hong, K.-B. Hong, *et al.*, "Perovskite random lasers: a tunable coherent light source for emerging applications," *Nanotechnology* **32**, 282001 (2021).
32. A. N. Azmi, W. Z. W. Ismail, H. A. Hassan, *et al.*, "Review of open cavity random lasers as laser-based sensors," *ACS Sens.* **7**, 914–928 (2022).
33. A. Yariv, A. Scherer, R. K. Lee, *et al.*, "Coupled-resonator optical waveguide: a proposal and analysis," *Opt. Lett.* **24**, 711–713 (1999).
34. V. N. Astratov, J. P. Franchak, and S. P. Ashili, "Optical coupling and transport phenomena in chains of spherical dielectric microresonators with size disorder," *Appl. Phys. Lett.* **85**, 5508–5510 (2004).
35. B. Möller, U. Woggon, and M. V. Artemyev, "Photons in coupled microsphere resonators," *J. Opt. A* **8**, S113–S121 (2006).
36. W. Ahn, X. Zhao, Y. Hong, *et al.*, "Low-power light guiding and localization in optoplasmonic chains obtained by directed self-assembly," *Sci. Rep.* **6**, 22621 (2016).
37. T. Mitsui, Y. Wakayama, T. Onodera, *et al.*, "Micro-demultiplexer of coupled resonator optical waveguide fabricated by microspheres," *Adv. Mater.* **22**, 3022–3026 (2010).
38. M. D. Barnes, S. M. Mahurin, A. Mehta, *et al.*, "Three-dimensional photonic 'molecules' from sequentially attached polymer-blend microparticles," *Phys. Rev. Lett.* **88**, 015508 (2001).
39. T. Mitsui, Y. Wakayama, T. Onodera, *et al.*, "Light propagation within colloidal crystal wire fabricated by a dewetting process," *Nano Lett.* **8**, 853–858 (2008).
40. M. Hossein-Zadeh and K. J. Vahala, "Fiber-taper coupling to whispering-gallery modes of a droplet resonator embedded in a liquid medium," in *Conference on Lasers and Electro-Optics* (Optical Society of America, 2006), paper CWI5.
41. A. Giorgini, S. Avino, P. Malara, *et al.*, "Fundamental limits in high-Q droplet microresonators," *Sci. Rep.* **7**, 41997 (2017).
42. Y. Wang, H. Li, L. Zhao, *et al.*, "A review of droplet resonators: operation method and application," *Opt. Laser Technol.* **86**, 61–68 (2016).
43. A. Kiraz, A. Kurt, M. A. Dündar, *et al.*, "Simple largely tunable optical microcavity," *Appl. Phys. Lett.* **89**, 081118 (2006).
44. S. Maayani and T. Carmon, "Droplet Raman laser coupled to a standard fiber," *Photon. Res.* **7**, 1188–1192 (2019).
45. A. Giorgini, S. Avino, P. Malara, *et al.*, "Stimulated Brillouin cavity optomechanics in liquid droplets," *Phys. Rev. Lett.* **120**, 073902 (2018).
46. S. Kaminski, L. L. Martin, S. Maayani, *et al.*, "Ripplon laser through stimulated emission mediated by water waves," *Nat. Photonics* **10**, 758–761 (2016).
47. L. Shang, Y. Cheng, and Y. Zhao, "Emerging droplet microfluidics," *Chem. Rev.* **117**, 7964–8040 (2017).
48. S. Liao, X. Tao, Y. Ju, *et al.*, "Multichannel dynamic interfacial printing: an alternative multicomponent droplet generation technique for lab in a drop," *ACS Appl. Mater. Interfaces* **9**, 43545–43552 (2017).
49. H.-T. Li, H.-F. Wang, Y. Wang, *et al.*, "A minimalist approach for generating picoliter to nanoliter droplets based on an asymmetrical beveled capillary and its application in digital PCR assay," *Talanta* **217**, 120997 (2020).
50. A. Ghaznavi, Y. Lin, M. Douvidzon, *et al.*, "A monolithic 3D printed axisymmetric co-flow single and compound emulsion generator," *Micromachines* **13**, 188 (2022).
51. L. I. Deych and O. Roslyak, "Photonic band mixing in linear chains of optically coupled microspheres," *Phys. Rev. E* **73**, 036606 (2006).
52. L. I. Deych, C. Schmidt, A. Chipouline, *et al.*, "Propagation of the fundamental whispering gallery modes in a linear chain of microspheres," *Appl. Phys. B* **93**, 21–30 (2008).
53. C.-S. Deng, H. Xu, and L. Deych, "Effect of size disorder on the optical transport in chains of coupled microspherical resonators," *Opt. Express* **19**, 6923–6937 (2011).
54. A. A. Savchenkov, A. B. Matsko, V. S. Ilchenko, *et al.*, "Direct observation of stopped light in a whispering-gallery-mode microresonator," *Phys. Rev. A* **76**, 023816 (2007).
55. T. Carmon, H. G. L. Schwefel, L. Yang, *et al.*, "Static envelope patterns in composite resonances generated by level crossing in optical toroidal microcavities," *Phys. Rev. Lett.* **100**, 103905 (2008).
56. S. T. Attar, V. Shuvayev, L. Deych, *et al.*, "Level-crossing and modal structure in microdroplet resonators," *Opt. Express* **24**, 13134–13141 (2016).

57. D. Bar-David, S. Maayani, L. L. Martin, *et al.*, "Cavity optofluidics: a μ droplet's whispering-gallery mode makes a μ vortex," *Opt. Express* **26**, 19115–19122 (2018).
58. M. L. Douvidzon, S. Maayani, L. L. Martin, *et al.*, "Light and capillary waves propagation in water fibers," *Sci. Rep.* **7**, 16633 (2017).
59. G. Roini, G. Calusi, M. Ferroni, *et al.*, "Nonlinear emission in CsPbBr₃ decorated metasurfaces," *Appl. Phys. Lett.* **122**, 241101 (2023).
60. T. Carmon, S. Y. T. Wang, E. P. Ostby, *et al.*, "Wavelength-independent coupler from fiber to an on-chip cavity, demonstrated over an 850 nm span," *Opt. Express* **15**, 7677–7681 (2007).
61. Y. Ren, R. Zhang, C. Ti, *et al.*, "Tapered optical fiber loops and helices for integrated photonic device characterization and microfluidic roller coasters," *Optica* **3**, 1205–1208 (2016).
62. Z. Chen, A. Taflove, and V. Backman, "Photonic nanojet enhancement of backscattering of light by nanoparticles: a potential novel visible-light ultramicroscopy technique," *Opt. Express* **12**, 1214–1220 (2004).
63. A. V. Itagi and W. A. Challener, "Optics of photonic nanojets," *J. Opt. Soc. Am. A* **22**, 2847–2858 (2005).
64. S. Lecler, Y. Takakura, and P. Meyrueis, "Properties of a three-dimensional photonic jet," *Opt. Lett.* **30**, 2641–2643 (2005).
65. S. Yang and V. N. Astratov, "Photonic nanojet-induced modes in chains of size-disordered microspheres with an attenuation of only 0.08dB per sphere," *Appl. Phys. Lett.* **92**, 261111 (2008).
66. Z. Chen, A. Taflove, and V. Backman, "Highly efficient optical coupling and transport phenomena in chains of dielectric microspheres," *Opt. Lett.* **31**, 389–391 (2006).
67. A. M. Kapitonov and V. N. Astratov, "Observation of nanojet-induced modes with small propagation losses in chains of coupled spherical cavities," *Opt. Lett.* **32**, 409–411 (2007).
68. K. W. Allen, A. Darafsheh, F. Abolmaali, *et al.*, "Microsphere-chain waveguides: focusing and transport properties," *Appl. Phys. Lett.* **105**, 021112 (2014).
69. A. V. Kanaev, V. N. Astratov, and W. Cai, "Optical coupling at a distance between detuned spherical cavities," *Appl. Phys. Lett.* **88**, 111111 (2006).
70. J. Fröhlich and T. Spencer, "A rigorous approach to Anderson localization," *Phys. Rep.* **103**, 9–25 (1984).
71. M. Tomes, K. J. Vahala, and T. Carmon, "Direct imaging of tunneling from a potential well," *Opt. Express* **17**, 19160–19165 (2009).